nature COMMUNICATIONS

ARTICLE

Received 6 Apr 2016 | Accepted 8 Jul 2016 | Published 9 Aug 2016

DOI: 10.1038/ncomms12496 OPEN

Force sensitivity of multilayer graphene optomechanical devices

P. Weber[1], J. Güttinger[1], A. Noury[1], J. Vergara-Cruz[1] & A. Bachtold[1]

Mechanical resonators based on low-dimensional materials are promising for force and mass sensing experiments. The force sensitivity in these ultra-light resonators is often limited by the imprecision in the measurement of the vibrations, the fluctuations of the mechanical resonant frequency and the heating induced by the measurement. Here, we strongly couple multilayer graphene resonators to superconducting cavities in order to achieve a displacement sensitivity of 1.3 fm $Hz^{-1/2}$. This coupling also allows us to damp the resonator to an average phonon occupation of 7.2. Our best force sensitivity, 390 zN $Hz^{-1/2}$ with a bandwidth of 200 Hz, is achieved by balancing measurement imprecision, optomechanical damping, and measurement-induced heating. Our results hold promise for studying the quantum capacitance of graphene, its magnetization, and the electron and nuclear spins of molecules adsorbed on its surface.

[1] ICFO-Institut de Ciencies Fotoniques, The Barcelona Institute of Science and Technology, Castelldefels (Barcelona) 08860, Spain. Correspondence and requests for materials should be addressed to A.B. (email: adrian.bachtold@icfo.es).

Considerable effort has been devoted to developing mechanical resonators based on low-dimensional materials, such as carbon nanotubes[1–12], semiconducting nanowires[13–22], graphene[23–29] and monolayer semiconductors[30–32]. The specificity of these resonators is their small size and their ultra-low mass, which enables sensing of force and mass with unprecedented sensitivities[7,10]. Such high-precision sensing capabilities hold promise for studying physical phenomena in new regimes that have not been explored thus far, for instance, in spin physics[33], quantum electron transport[34,35], light-matter interaction[19] and surface science[36,37]. However, the transduction of the mechanical vibrations of nanoscale mechanical systems into a measurable electrical or optical output signal is challenging. As a result, force and mass sensing is often limited by the imprecision in the measurement of the vibrations, and cannot reach the fundamental limit imposed by thermo-mechanical noise.

A powerful method to obtain efficient electrical readout of small resonators is to amplify the interaction between mechanical vibrations and the readout field using a superconducting microwave cavity[27–29]. Increasing the field in the cavity improves the readout sensitivity and eventually leads to dynamical back-action on the thermo-mechanical noise. This effect has been studied intensively on comparatively large micro-fabricated resonators, resulting for instance in enhanced optomechanical damping[38,39], ground-state cooling of mechanical vibrations[40,41] and displacement imprecision below the standard quantum limit[42,43]. Another phenomenon often observed when detecting and manipulating the motion of mechanical resonators is the induced heating that can occur through Joule dissipation and optical adsorption[28,44]. Heating is especially prominent in tiny mechanical resonators because of their small heat capacity. An additional difficulty in characterizing mechanical vibrations is related to the fluctuations of the mechanical resonant frequency, also called frequency noise, which are particularly sizable in small resonators endowed with high-quality factors Q[10].

Here we study the force sensitivity of multilayer graphene mechanical resonators coupled to superconducting cavities. In particular, we quantify how the force sensitivity is affected by dynamical back-action, Joule heating and frequency noise upon increasing the number of pump photons inside the cavity. We demonstrate a force sensitivity of $\left(S_F^{\rm tot}\right)^{1/2} = 390 \pm 30$ zN Hz$^{-1/2}$, of which $\approx$50% arises from thermo-mechanical noise and $\approx$50% from measurement imprecision. The force sensitivity tends to be limited by measurement imprecision and frequency noise at low pump power, and by optomechanical damping and Joule heating at high pump power.

Results

Thermal force noise and imprecision force noise. A fundamental limit of force sensing is set by the thermo-mechanical noise of the eigenmode that is measured. According to the fluctuation-dissipation theorem, the associated thermal force noise is white and is quantified by

$$S_F^{\rm mode} = 4k_{\rm B}T_{\rm mode}m_{\rm eff}\Gamma_{\rm eff}^{\rm spectral} \qquad (1)$$

where $T_{\rm mode}$ is the temperature of the mechanical eigenmode, and $m_{\rm eff}$ is its effective mass[8,45]. This force noise is transduced into a mechanical resonance with line width $\Gamma_{\rm eff}^{\rm spectral}$ and height $S_z^{\rm mode}$ in the displacement spectrum (Fig. 1). Importantly, equation (1) shows that the low mass of graphene decreases the size of the thermo-mechanical force noise. However, a drawback of tiny resonators with high Q-factors is their tendency to feature sizable frequency noise that broadens the resonance and, therefore, increases the size of the force noise[10,46].

Measuring mechanical vibrations with high accuracy is key to resolving small forces, since the imprecision in the measurement contributes to the force sensitivity. The force sensitivity $S_F^{\rm tot}$ is given by the sum of the thermal force noise $S_F^{\rm mode}$ and the imprecision force noise $S_F^{\rm imp}$, where the latter is the result of the white noise background with strength $S_z^{\rm imp}$ in the displacement spectrum (Fig. 1a). The challenge with mechanical resonators based on low-dimensional systems is to reach the limit $S_F^{\rm imp} < S_F^{\rm mode}$. When detecting the motion of graphene resonators with microwave cavities, one typically operates in the resolved sideband limit[27–29], where the cavity decay rate κ is significantly smaller than the mechanical resonance frequency $\omega_{\rm m}$. This is interesting for force sensing, because pumping on the red sideband allows to enhance the mechanical damping rate by $\Gamma_{\rm opt}$, and therefore to reduce the harmful effect of frequency noise, as we will discuss below. In addition, this allows to increase the measurement bandwidth, as is often done in magnetic resonance force microscopy experiments[33] while keeping $S_F^{\rm mode}$ constant. The drawback of red sideband pumping compared to pumping at the cavity resonant frequency is an increased imprecision force noise at high pump powers. In the red-detuned pump regime,

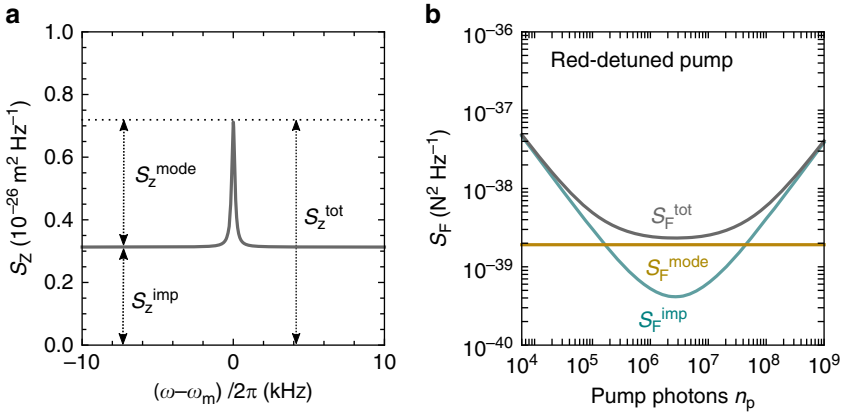

Figure 1 | Mechanical displacement and force sensitivity. (**a**) Mechanical displacement spectrum S_z close to the mechanical resonance frequency $\omega_{\rm m}/2\pi$. The total displacement spectral density $S_z^{\rm tot}$ at $\omega_{\rm m}$ is the sum of the displacement noise $S_z^{\rm mode}(\omega_{\rm m})$ and the displacement imprecision $S_z^{\rm imp}$. (**b**) Corresponding force sensitivity $S_{\rm F}^{\rm tot} = S_{\rm F}^{\rm mode} + S_{\rm F}^{\rm imp}$ (dark grey). The individual components are the thermal force noise $S_{\rm F}^{\rm mode}$ (dark yellow) and the imprecision force noise $S_{\rm F}^{\rm imp}$ (turquoise), given by equations (1) and (2), respectively. The quantum back-action noise is neglected for simplicity. For the plots most of the parameters are those of device B, but we estimate the mass assuming that the graphene flake is a single layer. Further we choose $n_{\rm add} = 0.5$, $T_{\rm bath} = 0.015$ K, and $n_{\rm p} = 2\cdot10^5$ in **a** (see text).

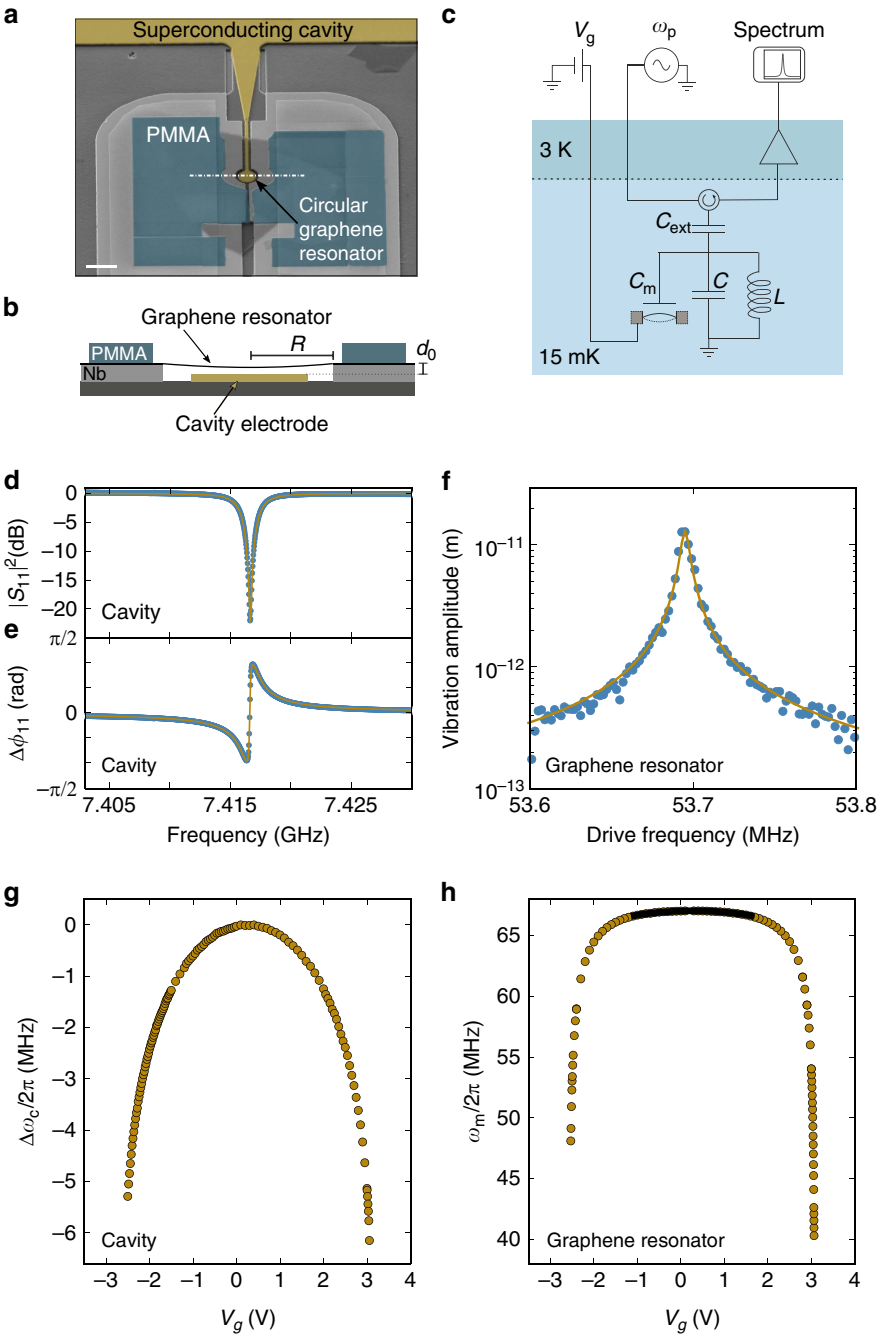

Figure 2 | Device and characterization. (**a**) False-colour image of the device. The cavity is coloured in dark yellow. The graphene flake is clamped in between niobium support electrodes (grey) and cross-linked poly(methyl metacrylate) (turquoise). The scale bar is 5 μm. (**b**) Schematic cross-section of the graphene resonator along the white dashed dotted line in **a**. (**c**) Schematic of the measurement circuit. The graphene mechanical resonator is coupled to the superconducting LC cavity through the capacitance C_m. The separation d between the suspended graphene flake and the cavity counter electrode is controlled by the constant voltage V_g. The cavity is pumped with a pump tone at ω_p and the output signal is amplified at 3 K. (**d**) Reflection coefficient $|S_{11}|^2$ and (**e**) reflected phase $\Delta\phi_{11}$ of the superconducting cavity of device A at $V_g = 3.002$ V. The dark yellow lines are fits to the data using $\kappa_{int}/2\pi = 950$ kHz and $\kappa_{ext}/2\pi = 850$ kHz using equation (7) (see Methods). (**f**) Driven vibration amplitude of the graphene resonator of device A as a function of drive frequency. The driving voltage is 22 nV and $V_g = 3.002$ V. The dark yellow line is a lorentzian fit to the data. (**g**) Resonant frequency $\omega_c/2\pi$ of the superconducting cavity as a function of V_g. (**h**) Resonant frequency $\omega_m/2\pi$ of the graphene resonator as a function of V_g. The black line is the V_g dependence of ω_m expected from electrostatic softening (see Supplementary Note 1).

the measurement imprecision contributes to the force sensitivity by the amount

$$S_F^{imp} = \hbar\omega_m m_{eff}\frac{\kappa}{\kappa_{ext}}\frac{\left(\Gamma_m^{spectral} + 4n_p g_0^2/\kappa\right)^2}{4n_p g_0^2/\kappa}\left(n_{add} + \frac{1}{2}\right), \quad (2)$$

with κ_{ext} the external coupling rate of the cavity, n_{add} the noise added by the amplifier chain at the output of the device, $\Gamma_m^{spectral}$ the intrinsic line width of the resonator, n_p the number of pump photons in the cavity, and g_0 the single-photon optomechanical coupling. Figure 1b shows the pump power dependence of the force sensitivity S_F^{tot} expected in the absence of Joule heating and frequency noise. The

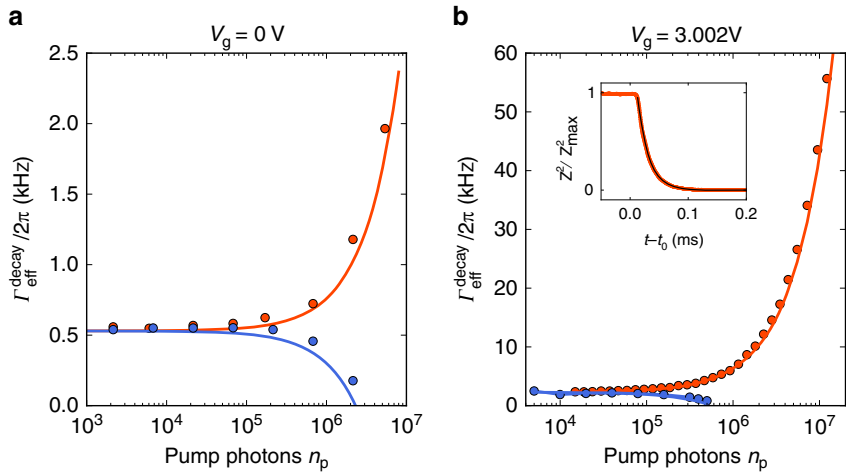

Figure 3 | Effective mechanical energy decay rates extracted from ring-down measurements. Mechanical dissipation rate Γ_{eff}^{decay} measured on device A with the ring-down technique as a function of the number n_p of pump photons in the cavity at $V_g = 0$ V and $V_g = 3.002$ V, where n_p is proportional to the microwave power P_{in} applied at the input of the cryostat (see Supplementary Note 3). Red and blue data points correspond to red and blue detuned pumping, respectively. The measurements are well described by $\Gamma_{eff}^{decay} = \Gamma_m^{decay} \pm \Gamma_{opt}$ (red and blue lines) using $g_0/2\pi = 9.7$ Hz in **a** and $g_0/2\pi = 42.6$ Hz in **b**. The inset in **b** shows a ring-down measurement for $n_p = 1.4 \cdot 10^6$. We plot the normalized vibration amplitude as a function of time t. The resonator is driven with a capacitive driving force for $t < t_0$. At t_0 the drive is switched off and the vibration amplitude decays freely ($t > t_0$). We fit the data with an exponential decay (black line) using $z^2(t) = z^2_{max} exp(-\frac{t-t_0}{\tau})$ with a decay rate $\Gamma_{eff}^{decay} = 1/\tau = 2\pi \cdot 8.4$ kHz. The vibration amplitude in ring-down measurements is larger than that in undriven displacement spectra, so that the motion in ring-down measurements can be resolved with lower n_p.

increase of S_F^{tot} at high n_p is due to the dynamical back-action, which enhances the mechanical line width by $\Gamma_{opt} = 4n_p g_0^2/\kappa$.

Device characterization. Our devices consist of a suspended graphene mechanical resonator capacitively coupled to a superconducting niobium (Nb) cavity (Fig. 2a–c). The graphene resonators are circular with a radius of $R \approx 1.6\,\mu$m. Here we present data of two devices. The graphene resonator of device A has a thickness of approximately 25 layers, and the one of device B 5–6 layers. This corresponds respectively to an effective mass of $m_{eff} = (4.1 \pm 0.8) \cdot 10^{-17}$ kg and $(9.6 \pm 0.8) \cdot 10^{-18}$ kg. The uncertainty results from extracting the mass with different methods including optical contrast measurements, thickness measurements with atomic force microscopy and the measured electrostatic softening of the mechanical resonators (see Supplementary Note 1 and Supplementary Equation 2). The fundamental mode of devices A and B vibrates at $\omega_m/2\pi = 67$ MHz and $\omega_m/2\pi = 46$ MHz at $V_g = 0$ V, respectively. Here V_g is the constant voltage applied between the graphene flake and the superconducting cavity. In order to improve the attachment of the graphene flake to its support, we clamp it between cross-linked poly(methyl metracylate) and the contact electrodes; the detailed fabrication is described elsewhere[29]. The separation between the graphene resonator and the cavity counter electrode at $V_g = 0$ V is assumed to be equal to the hole depth, which is typically $d_0 \approx 85$ nm in our devices as measured with atomic force microscopy. Varying V_g allows us to tune the separation between the graphene resonator and the cavity counter electrode[24,29,47–49], modifying the graphene-cavity capacitance, the cavity frequency ω_c and ω_m (Fig. 2g,h). The superconducting cavity is a coplanar waveguide resonating at about $\omega_c/2\pi = 7.4$ GHz. We choose a single-port, quarter wavelength, reflection geometry, so that the cavity is connected to ground on one end, allowing to apply a well-defined constant voltage between the cavity and the graphene flake. The other end of the cavity is coupled to a transmission line via a capacitor C_{ext} with a coupling rate $\kappa_{ext} = 2\pi \times 850$ kHz for device A; the total cavity decay rate is $\kappa = \kappa_{ext} + \kappa_{int} = 2\pi \times 1.8$ MHz (see Methods). Here κ_{int} accounts for the internal energy loss.

We detect the vibrations of the graphene resonator with high precision by pumping the cavity with an electromagnetic field, and probing its mechanical sideband. This sideband is generated by the capacitive modulation of the pump field at frequency $\omega_p/2\pi$ by the graphene vibrations at $\omega_m/2\pi$. We usually set $\omega_p = \omega_c - \omega_m$ and probe the electromagnetic field that exits the cavity at ω_c. We measure the device at the cryostat base temperature of 15 mK if not stated otherwise. The cavity output field is amplified with a high electron-mobility-transistor mounted at the 3 K stage of the cryostat. Mechanical noise spectra are detected with a spectrum analyser at room temperature. For a detailed description of the measurement set-up, see Supplementary Fig. 1 and Supplementary Note 2. In addition, we perform ring-down measurements to determine the mechanical dissipation rate Γ_{eff}^{decay} of the graphene resonator. Spectral measurements are not suitable for quantifying reliably Γ_{eff}^{decay} because of the potentially substantial frequency noise of graphene resonators.

We characterize the single-photon optomechanical coupling and show that the coupling can be significantly enhanced by deflecting the membrane towards the cavity electrode. For this, we quantify the optomechanical scattering rate Γ_{opt} using ring-down measurements at $V_g = 0$ V and $V_g = 3.002$ V for device A. Figure 3a,b shows the measured dissipation rate Γ_{eff}^{decay} as a function of cavity pump photon number n_p for blue and red detuned pumping. The measurements are well described by $\Gamma_{eff}^{decay} = \Gamma_m^{decay} \pm \Gamma_{opt}$ where Γ_m^{decay} corresponds to the intrinsic mechanical dissipation rate, and $\pm$ to red and blue detuned pumping at $\omega_p = \omega_c \mp \omega_m$, respectively. By increasing V_g from 0 to 3.002 V we obtain a strong increase of the optomechanical coupling from $g_0 = 2\pi \times 9.7$ Hz to $g_0 = 2\pi \times 42.6$ Hz. We estimate that the separation d between the membrane and the cavity counter electrode is reduced from 88 to 33 nm when varying V_g from 0 to 3.002 V. The calibration of both g_0 and n_p is robust, while the quantification of the reduction of d is approximative;

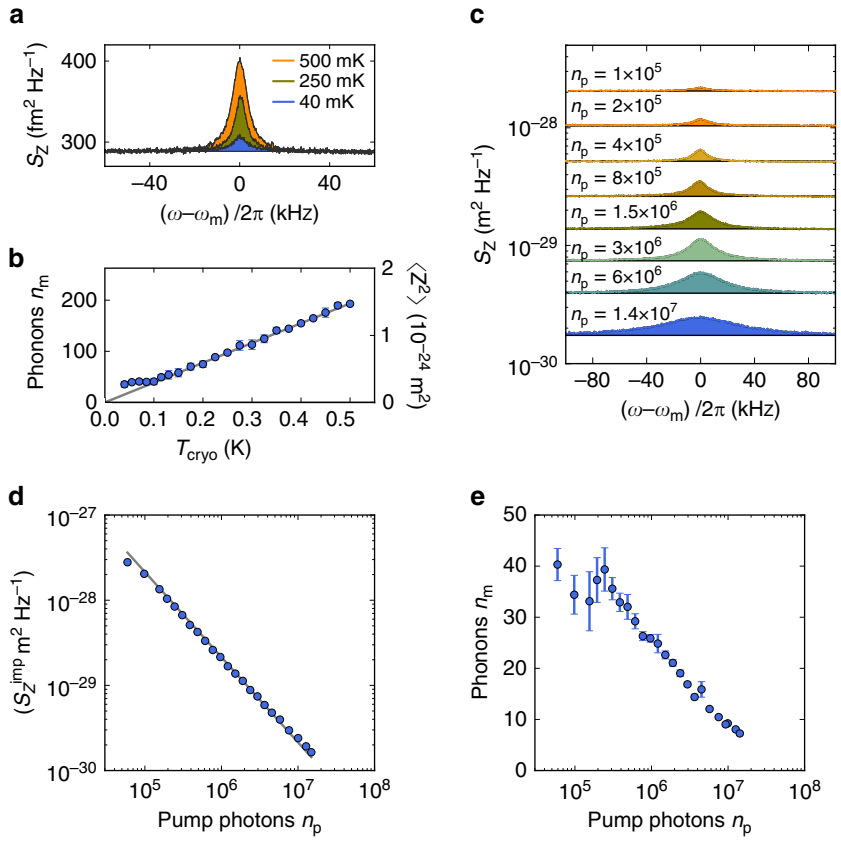

Figure 4 | Thermal calibration and sideband cooling of fundamental mechanical mode with red-detuned pumping. (**a**) Selected thermo-mechanical noise spectra for different temperatures and $n_p = 6\cdot10^4$. (**b**) Plot of the measured mechanical mode temperature of device A, expressed in phonon occupation n_m, as a function of cryostat temperature at $V_g = 3.002$ V where $\omega_m/2\pi = 53.7$ MHz and $n_p = 6\cdot10^4$. On the right y-axis, we display the variance of the vibration amplitude $\langle z^2\rangle$, which is obtained by integrating the thermal resonance, as is shown in **a**. The phonon occupation is quantified with $\langle z^2\rangle = (\hbar/m_{eff}\omega_m)n_m$ (see Supplementary Note 3). The error bars are given by the standard deviation of 5 spectral measurements. (**c**) Mechanical displacement spectral density S_z measured for different pump photon number. The cryostat temperature is 15 mK. Note that the curves are not offset. (**d**) Displacement imprecision as a function of cavity pump photon population. The line is a fit of equation (3) with $n_{add} = 32$. (**e**) Average phonon number n_m as a function of n_p. The error bars are given by the standard deviation of five spectral measurements.

see Supplementary Notes 1 and 3, Supplementary Fig. 2 and Supplementary equations (1), (3)–(5).

Thermal calibration and sideband cooling. In order to calibrate the mechanical phonon occupation and the mode temperature T_{mode}, we measure the mechanical thermal motion spectrum while varying the cryostat temperature[40]. This is done by pumping the cavity with a weak pump tone on the red sideband. The integrated area of the thermal resonance is proportional to the mode temperature according to the equipartition theorem. For temperatures above 100 mK the area is linearly proportional to the cryostat temperature, showing that the mode is in thermal equilibrium with the cryostat (Fig. 4b). This linear dependence serves as a precise calibration to relate the resonance area to the averaged phonon occupation n_m and the mode temperature T_{mode}. Below 100 mK the mechanical mode does not thermalize well with the cryostat. The origin of this poor thermalization at low temperature may be related to the heating induced by the pump field (see below)[28], and a non-thermal force noise[50] such as the electrostatic force noise related to the voltage noise in the device. As a next characterization step, we investigate the mechanical phonon occupation when increasing the power of the pump tone on the red sideband and keeping the temperature of the cryostat constant at $T_{cryo} = 15$ mK. The measured resonance gets broader and its area smaller (Fig. 4c), showing that the mechanical mode is damped and cooled[38,39]. At the largest available pump power, the phonon occupation reaches $n_m = 7.2 \pm 0.2$ (Fig. 4e). This is the lowest phonon occupation reached in a mechanical resonator based on graphene[27,28,51]. The error in the estimation of n_m is given by the standard error obtained from five successive spectral measurements.

Displacement sensitivity and force sensitivity. The improved coupling allows us to achieve also an excellent displacement sensitivity S_z^{imp} (Fig. 4d). At the largest pump power, we obtain $(S_F^{imp})^{1/2} = 1.3 \pm 0.2$ fm Hz$^{-1/2}$, which compares favourably to previous works[27,51,52]. The error in S_z^{imp} is given by the uncertainty in the estimation of m_{eff}. We obtain S_z^{imp} from the noise floor of the measured power spectral density S_N using $S_z^{imp} = \frac{S_N}{\hbar\omega_c}\frac{\kappa}{2\kappa_{ext}}\frac{z_{zp}^2}{g_0^2}\frac{1}{n_p}$ with $z_{zp} = \sqrt{\hbar/2m_{eff}\omega_m}$ the zero-point motion amplitude[27]. The displacement sensitivity scales as $1/n_p$ (Fig. 4d). By comparing the measurement to the expected displacement sensitivity

$$S_z^{imp} = \left(n_{add} + \frac{1}{2}\right)\frac{\kappa^2}{2\kappa_{ext}}\frac{z_{zp}^2}{g_0^2}\frac{1}{n_p}, \qquad (3)$$

we obtain that the equivalent noise added by the amplifier chain is $n_{add} = 32$. This is a reasonable value for a high electron-mobility-transistor amplifier mounted at 3 K[42,53].

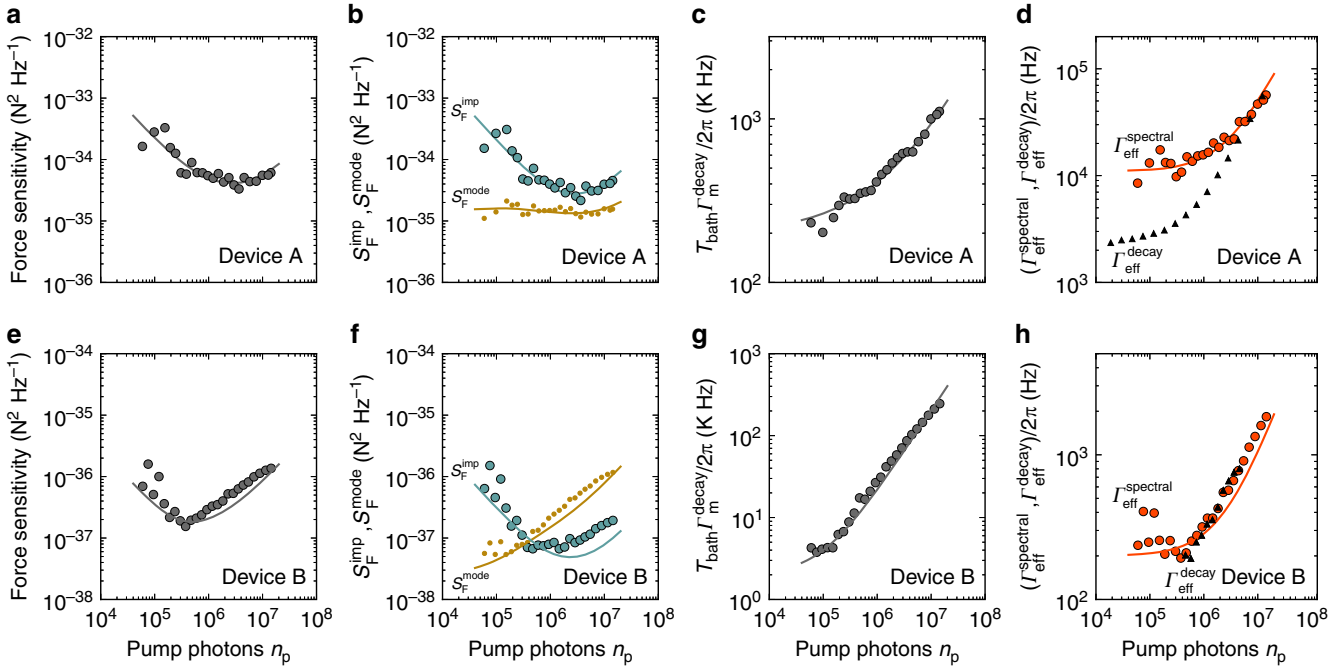

Figure 5 | Characterization of the force sensitivity. (**a**) Force sensitivity $S_F^{tot} = S_F^{imp} + S_F^{mode}$ as a function of cavity pump photon population measured when pumping the cavity on the red sideband. (**b**) Imprecision force noise S_F^{imp} (turquoise) and thermal force noise S_F^{mode} (dark yellow) versus n_p. The data in **a**,**b** are fitted to equations (2), (6). (**c**) Product of the bath temperature T_{bath} and the intrinsic mechanical decay rate Γ_m^{decay} as a function of cavity pump photon occupation. The line is a fit to the data. (**d**) Effective spectral mechanical line width $\Gamma_{eff}^{spectral}$ and energy decay Γ_{eff}^{decay} as a function of n_p. The data are fitted to $\Gamma_{eff}^{spectral} = \Gamma_{eff}^{decay} + \delta\Gamma_{noise}$ with $\delta\Gamma_{noise}/2\pi = 8.7$ kHz (red line). (**e**–**h**) Equivalent to (**a**–**d**) but for device B. The lowest value for the force sensitivity in **e** is $(S_F^{tot})^{1/2} = 390 \pm 30$ zN Hz$^{-1/2}$. In **e** and **f** the data are fitted with $n_{add} = 22$ and in **h** we use $g_0/2\pi = 7.3$ Hz, $\kappa/2\pi = 2.5$ MHz and $\delta\Gamma_{noise}/2\pi = 0.145$ kHz. All the measurements on device A are performed at $V_g = 3.002$ V and on device B at $V_g = 0$ V. The cryostat temperature is 15 mK.

We now quantify the force sensitivity as a function of the microwave pump power (Fig. 5a,e). Since the mechanical resonances in the measured displacement spectra are well described by Lorentzian line shapes, the thermal force noise is quantified using $S_F^{mode} = S_z^{mode}(\omega_m)/|\chi(\omega_m)|^2$ with the effective mechanical susceptibility $|\chi(\omega_m)|^2 = 1/(m_{eff}\omega_m\Gamma_{eff}^{spectral})^2$. Similarly, we obtain the imprecision force noise with $S_F^{imp} = S_z^{imp}/|\chi(\omega_m)|^2$. The best force sensitivity we achieve for device A is $(S_F^{tot})^{1/2} = 5.8$ aN Hz$^{-1/2}$ with a mechanical bandwidth of 20 kHz (Fig. 5a,d). In device B we reach a force sensitivity of $(S_F^{tot})^{1/2} = 390 \pm 30$ zN Hz$^{-1/2}$ with a mechanical bandwidth of 0.2 kHz (see Fig. 5e,h). The error in the estimation of the force sensitivity is obtained from both the uncertainty in the mass and the fluctuations in the measurement of S_F^{tot}, which we evaluate by calculating the standard error of 10 measurements. This force sensitivity compares favourably with the best sensitivities obtained with micro-fabricated resonators ($(S_F^{tot})^{1/2} = 510$ zN Hz$^{-1/2}$)[42,45], albeit it is not as good as that of resonators based on carbon nanotubes[8,10]. Compared to previous devices, the mechanical bandwidth of graphene resonators is much higher, which enables faster detection of sudden force changes.

Discussion

We plot both S_F^{mode} and S_F^{imp} as a function of cavity pump photon population in Fig. 5b. As expected, the imprecision force noise decreases at low n_p and increases at high n_p due to the enhanced damping caused by the optomechanical back-action. The thermal force noise S_F^{mode} appears roughly constant when varying n_p as a result of the competing effects of Joule heating and frequency noise. Joule heating is caused by the microwave current in the graphene flake induced by the pump field. This results in the increase of the temperature T_{bath} of the thermal bath coupled to the mechanical mode as well as the mechanical dissipation rate[26,28]. We can infer the product $T_{bath} \cdot \Gamma_m^{decay}$ from the measurements of n_m and Γ_{eff}^{decay} in Figs 3b and 4e using

$$T_{bath}\Gamma_m^{decay} = T_{mode}\Gamma_{eff}^{decay} = n_m\Gamma_{eff}^{decay} \cdot \frac{\hbar\omega_m}{k_B} \qquad (4)$$

When increasing the pump power, Joule heating significantly increases the product $T_{bath}\Gamma_m^{decay}$ (Fig. 5c), and therefore the size of the thermal force noise (equation (1)). We see next that the effect of frequency noise leads to the opposite dependence of the thermal force noise on pump power. Frequency noise enhances the spectral line width by the amount $\delta\Gamma_{noise}$,

$$\Gamma_{eff}^{spectral} = \Gamma_{eff}^{decay} + \delta\Gamma_{noise} \qquad (5)$$

when the fluctuations of the resonant frequency are described by a white noise[8]. The measurements of $\Gamma_{eff}^{spectral}$ and Γ_{eff}^{decay} as a function of pump power can be well described by equation (5) with $\delta\Gamma_{noise}/2\pi = 8.7$ kHz (Fig. 5d). Importantly, Fig. 5d shows that $\Gamma_{eff}^{spectral}$ is comparable to Γ_{eff}^{decay} at large pump power, showing that the relative contribution of $\delta\Gamma_{noise}$ to $\Gamma_{eff}^{spectral}$ gets negligible upon increasing n_p. As the cooling efficiency described by equation (4) remains unaltered by

frequency noise (see chapter 7 in[54]), the thermal force noise is quantified by

$$S_F^{mode} = 4k_B m_{eff} T_{bath} \Gamma_m^{decay} \frac{\Gamma_{eff}^{spectral}}{\Gamma_{eff}^{decay}} \quad (6)$$

Taking into account the measured effects of Joule heating and frequency noise in equation (6), the thermal force noise S_F^{mode} is expected to remain roughly constant as a function of n_p (dark yellow line in Fig. 5b), in agreement with the measurements. Overall, the best force sensitivity we achieve in this device is $\left(S_F^{tot}\right)^{1/2} = 5.8\,\mathrm{aN\,Hz^{-1/2}}$ at $n_p \approx 4 \cdot 10^6$ (Fig. 5a). While the force sensitivity in this device is primarily limited by the measurement imprecision, the thermal force noise is affected to a large extent by frequency noise at low n_p and by Joule heating at high n_p.

In device B, the graphene resonator has a lower mass and a narrower mechanical line width, two assets for high force sensitivity (Fig. 5e–h). The spectral line width corresponds to a mechanical quality factor of $Q \approx 200{,}000$. In this device we reach a force sensitivity of $\left(S_F^{tot}\right)^{1/2} = 390 \pm 30\,\mathrm{zN\,Hz^{-1/2}}$ at $n_p \approx 4 \cdot 10^5$ (see Fig. 5e). In an attempt to improve the thermal anchoring of device B compared to device A, the graphene contact electrodes contain an additional Au layer between the graphene and the Nb layer[28,55]. The normal metal layer is expected to increase the thermal conductance between the graphene flake and the contact electrodes through electron diffusion, which allows for better heat dissipation into the contacts. However, device B is still strongly affected by Joule heating, which substantially increases the value of S_F^{mode} when increasing the pump power (Fig. 5f,g). The heating is so strong that we are not able to reduce the phonon occupation n_m with sideband cooling. We attribute the strong heating to the fact that the resonator is significantly thinner than the one of device A and therefore has a smaller heat capacity. The effect of frequency noise on the spectral line width is negligible for pump powers above $n_p \approx 4 \cdot 10^5$. We do not know the origin of the frequency noise but it might be related to charged two-level fluctuators in the device. The force sensitivity is here primarily limited by the measurement imprecision at low n_p, and by the thermo-mechanical force noise and Joule heating at high n_p.

In the future, the force sensitivity of graphene optomechanical devices can be further improved using a quantum-limited Josephson parametric amplifier[53]. This readout will improve the measurement imprecision, by lowering n_{add} in S_F^{imp}. In addition, it will be possible to resolve the thermal vibrations with lower pump power, which is crucial to reduce Joule heating while working with low-mass graphene resonators. A quantum-limited amplifier with $n_{add} = 0.5$ may allow to achieve $47\,\mathrm{zN\,Hz^{-1/2}}$ force sensitivity at 15 mK taking the mass of a single-layer graphene resonator with the diameter and the quality factor of device B (Fig. 1b). With only modest device improvements, it may be possible to probe the fundamental limit of continuous displacement detection imposed by quantum mechanics, since the force noise associated to quantum backaction $\left(S_F^{qba}\right)^{1/2} = \left(2\hbar\omega_m m_{eff}\Gamma_{eff}^{decay}\right)^{1/2} = 1.1\,\mathrm{aN\,Hz^{-1/2}}$ is approaching $\left(S_F^{mode}\right)^{1/2} = 4.3\,\mathrm{aN\,Hz^{-1/2}}$ measured at $n_p = 1.4 \times 10^7$ for device A. Force sensing with resonators based on two-dimensional materials hold promise for detecting electron and nuclear spins[33] using superconducting cavities compatible with relatively large magnetic fields[56], and studying the thermodynamic properties of two-dimensional materials, such as the quantum capacitance and the magnetization[35].

Methods

Cavity characterization. In Fig. 2d,e we plot the coefficient $|S_{11}|^2$ and the phase of the reflected signal when sweeping the frequency over the cavity resonance at $\omega_c/2\pi = 7.416$ GHz. To extract the external coupling rate κ_{ext} and the internal loss rate κ_{int} we fit the measurement with the line shape expected for a one-port reflection cavity[57]

$$S_{11} = \frac{\kappa_{int} - \kappa_{ext} - 2i(\omega - \omega_c)}{\kappa_{int} + \kappa_{ext} - 2i(\omega - \omega_c)} \quad (7)$$

which yields $\kappa_{int}/2\pi = 950$ kHz and $\kappa_{ext}/2\pi = 850$ kHz at $V_g = 3.002$ V for device A. The rates of Device B are $\kappa_{int}/2\pi = 800$ kHz and $\kappa_{ext}/2\pi = 1700$ kHz at $V_g = 0$ V.

Data availability. The data that support the findings of this study are available from the corresponding author upon request.

References

1. Sazonova, V. *et al.* A tunable carbon nanotube electromechanical oscillator. *Nature* **431,** 284–287 (2004).
2. Jensen, K., Kim, K. & Zettl, A. An atomic-resolution nanomechanical mass sensor. *Nat. Nanotech.* **3,** 533–537 (2008).
3. Chiu, H. Y., Hung, P., Postma, H. W. C. & Bockrath, M. Atomic-scale mass sensing using carbon nanotube resonators. *Nano Lett.* **8,** 4342–4346 (2008).
4. Lassagne, B., Tarakanov, Y., Kinaret, J., Garcia-Sanchez, D. & Bachtold, A. Coupling mechanics to charge transport in carbon nanotube mechanical resonators. *Science* **325,** 1107–1110 (2009).
5. Steele, G. A. *et al.* Strong coupling between single-electron tunneling and nanomechanical motion. *Science* **325,** 1103–1107 (2009).
6. Gouttenoire, V. *et al.* Digital and FM demodulation of a doubly clamped single-walled carbon-nanotube oscillator: towards a nanotube cell phone. *Small* **6,** 1060–1065 (2010).
7. Chaste, J. *et al.* A nanomechanical mass sensor with yoctogram resolution. *Nat. Nanotech.* **7,** 301–304 (2012).
8. Moser, J. *et al.* Ultrasensitive force detection with a nanotube mechanical resonator. *Nat. Nanotech.* **8,** 493–496 (2013).
9. Ganzhorn, M., Klyatskaya, S., Ruben, M. & Wernsdorfer, W. Strong spin-phonon coupling between a single-molecule magnet and a carbon nanotube nanoelectromechanical system. *Nat. Nanotech.* **8,** 165–169 (2013).
10. Moser, J., Eichler, A., Güttinger, J., Dykman, M. I. & Bachtold, A. Nanotube mechanical resonators with quality factors of up to 5 million. *Nat. Nanotech.* **9,** 1007–1011 (2014).
11. Benyamini, A., Hamo, A., Kusminskiy, S. V., von Oppen, F. & Ilani, S. Real-space tailoring of the electron-phonon coupling in ultraclean nanotube mechanical resonators. *Nat. Phys.* **10,** 151–156 (2014).
12. Häkkinen, P., Isacsson, A., Savin, A., Sulkko, J. & Hakonen, P. Charge sensitivity enhancement via mechanical oscillation in suspended carbon nanotube devices. *Nano Lett.* **15,** 1667–1672 (2015).
13. Ayari, A. *et al.* Self-oscillations in field emission nanowire mechanical resonators: a nanometric dc-ac conversion. *Nano Lett.* **7,** 2252–2257 (2007).
14. Gil-Santos, E. *et al.* Nanomechanical mass sensing and stiffness spectrometry based on two-dimensional vibrations of resonant nanowires. *Nat. Nanotech.* **5,** 641–645 (2010).
15. Arcizet, O. *et al.* A single nitrogen-vacancy defect coupled to a nanomechanical oscillator. *Nat. Phys.* **7,** 879–883 (2011).
16. Nichol, J. M., Hemesath, E. R., Lauhon, L. J. & Budakian, R. Nanomechanical detection of nuclear magnetic resonance using a silicon nanowire oscillator. *Phys. Rev. B* **85,** 054414 (2012).
17. Nichol, J. M., Naibert, T. R., Hemesath, E. R., Lauhon, L. J. & Budakian, R. Nanoscale Fourier-transform magnetic resonance imaging. *Phys. Rev. X* **3,** 031016 (2013).
18. Sansa, M., Fernández-Regúlez, M., Llobet, L., San Paulo, A. & Pérez-Murano, F. High-sensitivity linear piezoresistive transduction for nanomechanical beam resonators. *Nat. Commun.* **5,** 4313 (2014).
19. Gloppe, A. *et al.* Bidimensional nano-optomechanics and topological backaction in a non-conservative radiation force field. *Nat. Nanotech.* **9,** 920–926 (2014).
20. Montinaro, M. *et al.* Quantum dot opto-mechanics in a fully self-assembled nanowire. *Nano Lett.* **14,** 4454–4460 (2014).
21. Mathew, J. P. *et al.* Nanoscale electromechanics to measure thermal conductivity, expansion, and interfacial losses. *Nano Lett.* **15,** 7621–7626 (2015).
22. Nigues, A., Siria, A. & Verlot, P. Dynamical backaction cooling with free electrons. *Nat. Commun.* **6,** 8104 (2015).
23. Bunch, J. S. *et al.* Electromechanical resonators from graphene sheets. *Science* **315,** 490–493 (2007).
24. Chen, C. *et al.* Performance of monolayer graphene nanomechanical resonators with electrical readout. *Nat. Nanotech.* **4,** 861–867 (2009).

25. Eichler, A. *et al.* Nonlinear damping in mechanical resonators made from carbon nanotubes and graphene. *Nat. Nanotech.* **6,** 339–342 (2011).
26. Miao, T., Yeom, S., Wang, P., Standley, B. & Bockrath, M. Graphene nanoelectromechanical systems as stochastic-frequency oscillators. *Nano Lett.* **14,** 2982–2987 (2014).
27. Singh, V. *et al.* Optomechanical coupling between a multilayer graphene mechanical resonator and a superconducting microwave cavity. *Nat. Nanotech.* **9,** 820–824 (2014).
28. Song, X., Oksanen, M., Li, J., Hakonen, P. J. & Sillanpää, M. A. Graphene optomechanics realized at microwave frequencies. *Phys. Rev. Lett.* **113,** 027404 (2014).
29. Weber, P., Güttinger, J., Tsioutsios, I., Chang, D. E. & Bachtold, A. Coupling graphene mechanical resonators to superconducting microwave cavities. *Nano Lett.* **14,** 2854–2860 (2014).
30. Lee, J., Wang, Z., He, K., Shan, J. & Feng, P. X. L. High frequency MoS2 nanomechanical resonators. *ACS Nano* **7,** 6086–6091 (2013).
31. van Leeuwen, R., Castellanos-Gomez, A., Steele, G. A., van der Zant, H. S. J. & Venstra, W. J. Time-domain response of atomically thin MoS2 nanomechanical resonators. *Appl. Phys. Lett.* **105,** 041911 (2014).
32. Wang, Z. & Feng, P. X. L. Dynamic range of atomically thin vibrating nanomechanical resonators. *Appl. Phys. Lett.* **104,** 103109 (2014).
33. Rugar, D., Budakian, R., Mamin, H. J. & Chui, B. W. Single spin detection by magnetic resonance force microscopy. *Nature* **430,** 329–332 (2004).
34. Bleszynski-Jayich, A. C. *et al.* Persistent currents in normal metal rings. *Science* **326,** 272–275 (2009).
35. Chen, C. *et al.* Modulation of mechanical resonance by chemical potential oscillation in graphene. *Nat. Phys.* **12,** 240–244 (2016).
36. Wang, Z. *et al.* Phase transitions of adsorbed atoms on the surface of a carbon nanotube. *Science* **327,** 552–555 (2010).
37. Tavernarakis, A. *et al.* Atomic monolayer deposition on the surface of nanotube mechanical resonators. *Phys. Rev. Lett.* **112,** 196103 (2014).
38. Arcizet, O., Cohadon, P. F., Briant, T., Pinard, M. & Heidmann, A. Radiation-pressure cooling and optomechanical instability of a micromirror. *Nature* **444,** 71–74 (2006).
39. Gigan, S. *et al.* Self-cooling of a micromirror by radiation pressure. *Nature* **444,** 67–70 (2006).
40. Teufel, J. *et al.* Sideband cooling of micromechanical motion to the quantum ground state. *Nature* **475,** 359–363 (2011).
41. Chan, J. *et al.* Laser cooling of a nanomechanical oscillator into its quantum ground state. *Nature* **478,** 89–92 (2011).
42. Teufel, J. D., Donner, T., Castellanos-Beltran, M. A., Harlow, W. J. & Lehnert, K. W. Nanomechanical motion measured with an imprecision below that at the standard quantum limit. *Nat. Nanotech.* **4,** 820–823 (2009).
43. Anetsberger, G. *et al.* Measuring nanomechanical motion with an imprecision below the standard quantum limit. *Phys. Rev. A* **82,** 061804 (2010).
44. Meenehan, S. M. *et al.* Silicon optomechanical crystal resonator at millikelvin temperatures. *Phys. Rev. A* **90,** 011803 (2014).
45. Mamin, H. J. & Rugar, D. Sub-attonewton force detection at millikelvin temperatures. *Appl. Phys. Lett.* **79,** 3358 (2001).
46. Zhang, Y., Moser, J., Güttinger, J., Bachtold, A. & Dykman, M. I. Interplay of driving and frequency noise in the spectra of vibrational systems. *Phys. Rev. Lett.* **113,** 255502 (2014).
47. Singh, V. *et al.* Probing thermal expansion of graphene and modal dispersion at low-temperature using graphene nanoelectromechanical systems resonators. *Nanotechnology* **21,** 165204 (2010).
48. Bao, W. *et al. In situ* observation of electrostatic and thermal manipulation of suspended graphene membranes. *Nano Lett.* **12,** 5470–5474 (2012).
49. Chen, C. *et al.* Graphene mechanical oscillators with tunable frequency. *Nat. Nanotech.* **8,** 923–927 (2013).
50. Rocheleau, T. *et al.* Preparation and detection of a mechanical resonator near the ground state of motion. *Nature* **463,** 72–75 (2009).
51. Barton, R. A. *et al.* Photothermal self-oscillation and laser cooling of graphene optomechanical systems. *Nano Lett.* **12,** 4681–4686 (2012).
52. Cole, R. M. *et al.* Evanescent-field optical readout of graphene mechanical motion at room temperature. *Phys. Rev. Appl.* **3,** 024004 (2015).
53. Castellanos-Beltran, M., Irwin, K., Hilton, G., Vale, L. & Lehnert, K. Amplification and squeezing of quantum noise with a tunable Josephson metamaterial. *Nat. Phys.* **4,** 929–931 (2008).
54. Dykman, M. I. (ed). *Fluctuating Nonlinear Oscillators* (Oxford, 2012).
55. Fong, K. C. *et al.* Measurement of the electronic thermal conductance channels and heat capacity of graphene at low temperature. *Phys. Rev. X* **3,** 041008 (2013).
56. Samkharadze, N. *et al.* High-kinetic-inductance superconducting nanowire resonators for circuit QED in a magnetic field. *Phys. Rev. Appl.* **5,** 044004 (2016).
57. Aspelmeyer, M., Kippenberg, T. J. & Marquardt, F. Cavity optomechanics. *Rev. Mod. Phys.* **86,** 1391 (2014).

Acknowledgements

We thank P. Verlot and M. Dykman for discussions. We acknowledge financial support by the ERC starting grant 279278 (CarbonNEMS), the EE Graphene Flagship (contact no. 604391), from MINECO and the Fondo Europeo de Desarrollo Regional (FEDER) through grant MAT2012-31338 and FIS2015-69831-P, the Fundació Privada Cellex, the Severo Ochoa Excellence Grant, and the Generalitat through AGAUR.

Author contributions

P.W. fabricated the devices, the process being developed by P.W. and J.G. P.W., J.G. and A.N. carried out the experiment with support from J.V.C. The data analysis was done by P.W. and J.G. with inputs from A.B. The experimental setup was built by J.G. with support from P.W. P.W. and A.B. wrote the manuscript with comments from J.G. and A.N. A.B. and J.G. conceived the experiment and supervised the work.

Additional information

Supplementary Information accompanies this paper at http://www.nature.com/naturecommunications

Competing financial interests: The authors declare no competing financial interests.

Reprints and permission information is available at http://npg.nature.com/reprintsandpermissions/

How to cite this article: Weber P. *et al.* Force sensitivity of multilayer graphene optomechanical devices. *Nat. Commun.* 7:12496 doi: 10.1038/ncomms12496 (2016).